Direct observation of 2-dimensional ices on different surfaces near room temperature without confinement

Chongqin Zhu[a,b,c,1], Yurui Gao[c,1], Weiduo Zhu[c,d,e], Jian Jiang[c], Jie Liu[f,g], Jianjun Wang[f,g], Joseph S. Francisco[a,b,2], and Xiao Cheng Zeng[c,2]

[a]Department of Earth and Environmental Science, University of Pennsylvania, Philadelphia, PA 19104; [b]Department of Chemistry, University of Pennsylvania, Philadelphia, PA 19104; [c]Department of Chemistry, University of Nebraska–Lincoln, Lincoln, NE 68588; [d]Hefei National Laboratory for Physical Sciences at Microscale, University of Science and Technology of China, Hefei, 230026 Anhui, China; [e]Department of Chemical Physics, University of Science and Technology of China, Hefei, 230026 Anhui, China; [f]Key Laboratory of Green Printing, Institute of Chemistry, Chinese Academy of Sciences, 100190 Beijing, China; and [g]School of Chemistry and Chemical Engineering, University of Chinese Academy of Sciences, 100190 Beijing, China

Contributed by Joseph S. Francisco, June 27, 2019 (sent for review April 12, 2019; reviewed by Greg A. A. Kimmel and Xifan Wu)

Water–solid interfaces play important roles in a wide range of fields, including atmospheric science, geochemistry, electrochemistry, and food science. Herein, we report simulation evidence of 2-dimensional (2D) ice formation on various surfaces and the dependence of the 2D crystalline structure on the hydrophobicity and morphology of the underlying surface. Contrary to the prevailing view that nanoscale confinement is necessary for the 2D liquid-to-bilayer ice transition, we find that the liquid-to-bilayer hexagonal ice (BHI) transition can occur either on a model smooth surface or on model fcc-crystal surfaces with indices of (100), (110), and (111) near room temperature. We identify a critical parameter that characterizes the water–surface interaction, above which the BHI can form on the surface. This critical parameter increases as the temperature increases. Even at temperatures above the freezing temperature of bulk ice (I_h), we find that BHI can also form on a superhydrophilic surface due to the strong water–surface interaction. The tendency toward the formation of BHI without confinement reflects a proper water–surface interaction that can compensate for the entropy loss during the freezing transition. Furthermore, phase diagrams of 2D ice formation are described on the plane of the adsorption energy versus the fcc lattice constant (E_{ads}–a_{fcc}), where 4 monolayer square-like ices are also identified on the fcc model surfaces with distinct water–surface interactions.

2-dimensional ice | phase transition | 2-dimensional ice formation without confinement | bilayer hexagonal ice | surface hydrophobicity

Water–solid interactions are crucial in diverse everyday phenomena and are widely investigated in scientific and technological processes (1–14). Since water molecules near a solid surface can undergo stratification, both hydrophobic and hydrophilic surfaces can have a profound influence on the vicinal structure of a water film. Over the past 2 decades, many molecular dynamics (MD) simulations and a few experiments have shown the formation of 2-dimensional (2D) crystalline and amorphous ices when water confined between planar hydrophobic surfaces is slowly cooled (7, 15–27), a manifestation of the extraordinary ability of water molecules to form diverse hydrogen-bonding networks under nanoscale confinement. To date, it has been reported that water confined between 2 parallel surfaces can form monolayer and bilayer square ices (7, 15), distorted bilayer hexagonal ice (BHI) (16, 17), bilayer hexagonal and rhombic ices (18–21), bilayer interlocked pentagonal ice (22), monolayer rhombic ices (23, 24), trilayer ice (25), and trilayer heterogeneous fluid (26).

Recently, a number of studies revealed the exciting possibility of 2D ice formation on surfaces without the need of nanoscale confinement. For example, a previous study of a water–mica interface indicated the presence of an ice-like water layer (28–30). A sum-frequency generation experiment revealed no free OH bonds in the adsorbed water layer on mica (31). Kimmel et al. (32) experimentally demonstrated the formation of BHI via water vapor deposition on a graphene/Pt(111) substrate at temperatures between 100 and 135 K. Such a BHI structure was originally predicted to form when liquid water confined to a nanoscale slit is slowly cooled (16, 33). Later, the low-temperature growth of bilayer ice was also observed on an Au(111) substrate (34), a Pt(111) substrate (35), and a Ru(0001) substrate (35), all at extremely low temperatures (<140 K). The formation of bilayer ice on gold is attributed to the relatively weak interaction between gold and water (34). However, previous MD simulations show that when confined between hydrophobic surfaces, the BHI formed exhibits an anomalously high melting point, even higher than the computed melting temperature of bulk ice (I_h) (16, 33).

Despite much effort in studying the behavior of water/ice at the interface, the influence of the hydrophobicity and morphology of the surface on the formation of 2D ices without confinement has not been systematically studied. Here, we report a comprehensive simulation study of the formation of 2D ices on various model surfaces, particularly fcc-crystal surfaces with different morphologies, including the (111), (100), (110), and (211) surfaces, as well as surfaces with different strengths of water–surface interactions. For each surface considered, we built a dataset of 10 different slabs with the fcc lattice parameter a_{fcc} varying from 3.52 to 4.66 Å. Note that this lattice-parameter range encompasses several fcc metals, ranging from Ni to Ag, including the Pt structure. We show simulation evidence that BHI can form directly from liquid

Significance

Many metal surfaces can stabilize 2-dimensional (2D) water monolayers or various structures of 2D ices, depending on the temperature and metal surface structures. Understanding of 2D ice formation on different surfaces at the molecular level, however, remains incomplete. We report simulation evidence of 2D ice formation on various surfaces without confinement and dependence of the 2D structure of water on the hydrophobicity and structure of underlying surface. The direct transformation of water nanodroplets to different 2D ices is shown, either on a smooth model surface or on fcc-crystal surfaces near room temperature. Physical mechanism related to the formation of different 2D ices is elucidated, which offers deeper insight into how the 2D ice formation is related to the water–surface interactions.

Author contributions: C.Z., Y.G., J.S.F., and X.C.Z. designed research; C.Z., Y.G., W.Z., and J.J. performed research; J.S.F. and X.C.Z. contributed new reagents/analytic tools; C.Z., Y.G., W.Z., J.J., J.L., J.W., and X.C.Z. analyzed data; and C.Z., Y.G., J.S.F., and X.C.Z. wrote the paper.

Reviewers: G.A.A.K., Pacific Northwest National Laboratory; and X.W., Temple University.

The authors declare no conflict of interest.

[1]C.Z. and Y.G. contributed equally to this work.

[2]To whom correspondence may be addressed. Email: frjoseph@sas.upenn.edu or xzeng1@unl.edu.

This article contains supporting information online at www.pnas.org/lookup/suppl/doi:10.1073/pnas.1905917116/-/DCSupplemental.

water on a smooth surface and on 3 fcc crystal surfaces, i.e., (100), (110), and (111) surfaces, near room temperature without nanoscale confinement. This direct liquid–BHI transition is strongly dependent on the degree of hydrophobicity of the surface and the temperature. At a given temperature, there exists a critical parameter that characterizes the water–surface interaction, above which the liquid-to-BHI transition can be observed. Moreover, we identified 4 monolayer square-like ices that can also form on the fcc crystal surfaces. Our findings provide a molecular-level understanding of 2D ice formation on surfaces without confinement, thereby offering a guide for growing 2D ices on different solid surfaces.

Correlation between the Contact Angle and the Water–Surface Interaction

Prior to the MD simulations of 2D ice formation on a smooth surface, a series of classical MD simulations were performed to quantitatively determine the correlation between the contact angle (θ) of a water nanodroplet on the surface and the water–surface interaction parameter ε (*SI Appendix*, Fig. S1). *SI Appendix*, Fig. S2 shows a plot of $\cos\theta$ versus ε. Generally, as ε increases, θ decreases. When ε exceeds a critical value, water can completely wet the surface with $\theta = 0$. According to previous studies, $\cos\theta$ exhibits a linear dependence on ε (36). The solid red line in *SI Appendix*, Fig. S2 represents a linear fit of all data points (for $\theta > 0$) using the least-squares fitting method. The fitted straight line is given by

$$\cos\theta = 0.383\varepsilon - 1.477. \quad [1]$$

Formation of BHI on a Smooth Surface without Confinement

In the first series of MD simulations, for a fixed ε, the temperature was first lowered in steps until the freezing was observed and was then raised in steps until the melting was completed. *SI Appendix*, Fig. S3 shows the temperature dependence of the potential energy, excluding contribution from the water–wall interactions. In the series of MD simulations, with the system being cooled in 10-K/5-K steps, the potential energy gradually decreased first and then suddenly dropped by ~0.6 kcal/mol to a lower value. In the reverse heating series, the potential energy jumped to a higher value at a temperature higher than the transition temperature seen in the cooling series. This strong hysteresis shown in the potential energy curves indicates that the phase transition is strong first order.

Fig. 1*A* displays the variation in the potential energy (U^{WW}), excluding the contributions from the water–surface interactions, versus the water–surface interaction parameter ε for the equilibrium system at 250 K. As ε increases, the potential energy initially increases gradually and then suddenly drops by ~0.45 kcal/mol. This potential-energy drop occurs between ε = 5.22 kcal/mol (at which the adsorption energy of a single water molecule E_{ads} = −2.009 kcal/mol) and ε = 5.41 kcal/mol (E_{ads} = −2.082 kcal/mol), corresponding to contact angles $\theta = 58.5°$ and 53.5°, respectively. Thus, we estimate that the critical value of ε corresponding to the boundary, above which the solid phase is preferred, $\varepsilon^c = 5.315 \pm 0.095$ kcal/mol (corresponding to $E^c_{ads} = -2.045 \pm 0.037$ kcal/mol or $\theta^c = 56° \pm 2.5°$).

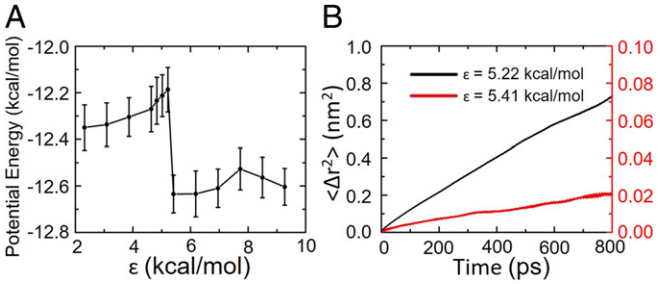

Fig. 1. (*A*) The potential energy per water molecule in a water slab versus water–surface interaction parameter (ε) on the surface at T = 250 K after equilibrium. The potential energy accounts for only the water–water intermolecular interactions (excluding the water–surface potential energy). (*B*) Mean-square displacement of water molecules in the *xy*-plane parallel to the model surface at 250 K, after a 30-ns MD simulation, for ε = 5.22 kcal/mol (black line) and ε = 5.41 kcal/mol (red line, corresponding to the red axis on the right).

Moreover, the self-diffusion constants in the *xy*-plane (D_{xy}) (37) below and above the boundary differ by 2 orders of magnitude ($D_{xy} = 2.7 \times 10^{-6}$ cm^2/s for ε = 5.22 kcal/mol and $D_{xy} = 4.2 \times 10^{-8}$ cm^2/s for ε = 5.41 kcal/mol), indicating that the 2 phases after equilibrium indeed correspond to a liquid and solid, respectively (Fig. 1B). Unlike previously reported BHI formation through vapor deposition on a surface at very low temperature (32, 34, 35), here, the formation of BHI on the surface occurs through a spontaneous liquid-to-solid transition near room temperature and is therefore insensitive to the value of low pressure used in the MD simulations (*SI Appendix*, Fig. S4).

Top views of the liquid and ice phases at T = 250 K are shown in Fig. 2 *A* and *B*, respectively. The solid has 2 layers, where the oxygen atoms in both layers (indicated by blue and red spheres) are in registry. A side view of the bilayer ice (Fig. 2*B*) and the transverse density profile (TDP) of the oxygen atoms (Fig. 2*C*) show that each layer of the ice is almost flat, consistent with previous studies (16, 33). Since the bilayer ice satisfies the Bernal–Fowler ice rules (no dangling proton exists in the bilayer ice), the Bjerrum defects (38) should play little role in the formation of the ice, especially considering the extremely low Bjerrum defect density in the bilayer ice (*SI Appendix*, section D). Overall, the bilayer ice exhibits a similar local network structure as the bilayer ice obtained with confinement (33), as well as that grown on Ru(0001) and Pt(111) (35). As shown in Fig. 2*B*, the hexagonal rings are the predominant local structure in the bilayer ice, although pentagonal, heptagonal, and octagonal rings can also be observed. To gain more insight into the structural features of the bilayer ice, we computed the oxygen atom radial distribution function (RDF), g_{OO}. As shown in Fig. 2*D*, at ε = 5.41 kcal/mol (red line), the sharp density maxima and minima validate the high structural order of the bilayer ice. Moreover, as shown in Fig. 2*E*, a broad distribution of the O–O–O angles with 2 main peaks located at 90° and 120° is observed due to the presence of not only hexagonal rings but also pentagonal, heptagonal, and octagonal rings. To rule out the influence of disproportion between the unit cells and periodically ordered ice structure, we performed 2 other sets of simulations: one in the $NP_{xy}T$ ensemble with a fixed load P_{xy} = 1 bar and another with larger system sizes. Snapshots (*SI Appendix*, Fig. S5) and the RDF (*SI Appendix*, Fig. S6) clearly show that bilayer ice can form on the surface. However, the number of pentagonal, heptagonal, and octagonal rings in the interior part of the bilayer ice decrease dramatically or even to zero with longer simulation time (*SI Appendix*, Fig. S7), which indicates that the mixture of hexagonal, pentagonal, and other rings represents local-minimum energy structures.

Independent simulations were also performed by using 3 other water models, TIP4P/2005 (39), monatomic water model mW (40), and HBP polarizable water model (41), to assure that the conclusions were not model-dependent (*SI Appendix*). Again, ε-dependent BHI formation was observed with the TIP4P/2005 model (*SI Appendix*, Fig. S8), monatomic water model (*SI Appendix*, Fig. S9), and HBP water model (*SI Appendix*, Fig. S10). In addition, another 2 independent series of MD simulations were performed to investigate the effect of size parameter σ on the formation of BHI (*SI Appendix*, section H). The simulation results showed that the liquid–solid transition is insensitive to the σ value (*SI Appendix*, Fig. S11).

Is it possible that the observed liquid–BHI transition is a prewetting transition (42, 43)? Note that the prewetting transitions of water were first studied by using Monte Carlo (MC) simulation

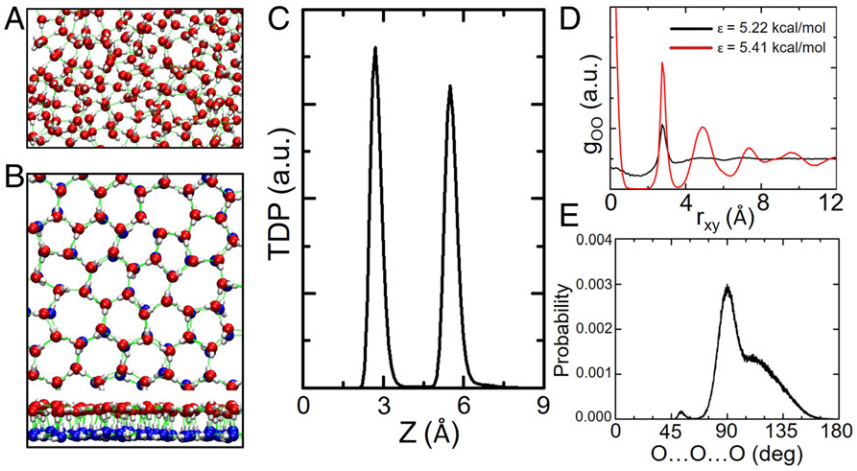

Fig. 2. Inherent structure of a water slab on a model surface at T = 250 K. (*A*) Top view of the snapshot of water film at the end of 30 ns on the surface for ε = 5.22 kcal/mol (liquid phase). (*B*) Top view (*Upper*) and side view (*Lower*) of the snapshot of water film at the end of 30 ns on the surface for ε = 5.41 kcal/mol (solid phase). Oxygen atoms are depicted as red and blue spheres, hydrogen atoms as white sticks, and hydrogen bonds as orange dotted lines. (*C*) TDP of oxygen atoms in ices near the model surface for ε = 5.41 kcal/mol and T = 250 K. (*D*) RDFs of the oxygen atoms of water on the surface for ε = 5.22 kcal/mol (black) and ε = 5.41 kcal/mol (red) and at T = 250 K. Distance r_{xy} is the distance in a plane parallel to the surface. (*E*) Distributions of nearest-neighbor O–O–O angles for ε = 5.41 kcal/mol and at T = 250 K in all MD simulations (30 ns) after the formation of bilayer ice. a.u., arbitrary units.

in the Gibbs ensemble (GE) with a homemade code (*SI Appendix*, section J and Figs. S12 and S13). After the GEMC simulations, the 2 bilayer phases were used as the initial configuration for further MD simulations in the $NP_{xy}T$ ensemble (P_{xy} = 1 bar) with different temperatures (*SI Appendix*, section K). The temperature dependence of the potential energy per water molecule in the water slab (*SI Appendix*, Fig. S14*A*), that of the diffusion coefficients (*SI Appendix*, Fig. S14*B*), and snapshots (*SI Appendix*, Fig. S15) all suggest a strong first-order phase transition from 2 water layers to BHI. Moreover, BHI no longer can be observed on the surface regardless of its hydrophilicity if $T > 237.5 \pm 2.5$ K for the conventional TIP4P water model, ~5 K higher than the melting temperature of bulk TIP4P ice (I_h) (229 ± 2 K). However, the prewetting transition can still be observed even at 300 K from our GEMC simulations (*SI Appendix*, Fig. S12).

Molecular Insight into the Formation of BHI without Confinement

To gain deeper insights into why surface wettability plays such an important role in BHI formation on a surface, we computed the interaction energy (U^{WS}) between water and the surface versus ε at T = 250 K (*SI Appendix*, Fig. S16). In the range of ε = 2.32–5.22 kcal/mol, U^{WS} first decreased gradually from −0.20 to −0.86 kcal/mol and then dropped suddenly by approximately 0.31 kcal/mol as ε increased from 5.22 to 5.41 kcal/mol. Such a sudden decrease in U^{WS} is a manifestation of the phase transition. Due to the flat structure of BHI, the interaction energy between water and the surface decreases as the liquid turns into a solid. Using the thermodynamic relation,

$$\mathrm{A} = U^{WW} + U^{WS} - TS, \qquad [2]$$

where A, T, S, and U^{WW} denote the Helmholtz free energy, absolute temperature, entropy of the system, and the potential energy accounts for the water–water intermolecular interactions, respectively. At a given ε and T, the difference in A between the solid and liquid is given by

$$\Delta\mathrm{A} = \left(U^{WW}_{solid} - U^{WW}_{liquid}\right) + \left(U^{WS}_{solid} - U^{WS}_{liquid}\right) - T\left(S_{solid} - S_{liquid}\right)$$

$$= \Delta U^{WW} + \Delta U^{WS} - T\Delta S. \qquad [3]$$

A small increase in ε is expected to lead to a significant decrease in ΔU^{WS}, while ΔU^{WW} and ΔS are expected to exhibit little variation at the same temperature. Therefore, when ε is sufficiently large, $\Delta A = 0$ can be obtained, corresponding to the occurrence of the phase transition. Note that during the phase transition, ΔU^{WW} and ΔU^{WS} are approximately equal to −0.45 kcal/mol $[U^{WW}_{solid}(\varepsilon = 5.41\ \mathrm{kcal/mol}) - U^{WW}_{liquid}(\varepsilon = 5.22\ \mathrm{kcal/mol})]$ and −0.31 kcal/mol $[U^{WS}_{solid}(\varepsilon = 5.41\ \mathrm{kcal/mol}) - U^{WS}_{liquid}(\varepsilon = 5.22\ \mathrm{kcal/mol})]$, respectively. Hence, the entropy difference (ΔS) between the bilayer ice and liquid is approximately −3.0 cal/(mol·K) at T = 250 K.

Another important aspect of physics is the temperature dependence of the critical value of ε^c—namely, the value of ε at which the liquid–solid phase transition occurs—especially considering that bilayer ice obtained with confinement has been reported to exhibit an anomalously high melting point (33). *SI Appendix*, Fig. S17 presents the calculated potential energy (U^{WW}), excluding the contribution from the water–surface interaction, versus ε at various temperatures. At T = 230 K, the sharp increase in U^{WW} at ε = 4.73 ± 0.10 kcal/mol indicates that the liquid transforms into a solid at this critical value of ε. ε^c increased gradually from 4.73 kcal/mol at 230 K to 6.86 kcal/mol at 275 K (Fig. 3). This range of ε^c corresponds to the adsorption energy E_{ads} of a single water molecule of approximately −2 kcal/mol. For comparison, the adsorption energies of a single water molecule on Pt(111), Ru(0001), Rh(111), and Pd(111) surfaces are −6.71, −9.43, −9.43, and −7.01 kcal/mol (44), respectively, all of which are much larger in magnitude than the critical adsorption energy. Notably, at 275 K, BHI can be observed on a superhydrophilic surface (ε > 6.86 kcal/mol); this temperature of 275 K is even higher than the freezing temperature of bulk TIP4P/ice (I_h) (268 ± 2 K) (45). However, when the temperature is higher than 277.5 ± 2.5 K, BHI can no longer be observed on the surface, even when the ε value is very large (9.27 kcal/mol). Lastly, the entropy difference between the bilayer ice and liquid water (ΔS) was calculated at various temperatures (*SI Appendix*, Table S1). ΔS is nearly independent of T and exhibits a constant value of 2.94 ± 0.18 cal/(mol·K).

Formation of 2D Ice on 4 Other Model Surfaces without Confinement

In addition to the smooth surface, we also investigated 2D ice formation on different atomic surfaces of an fcc crystal, i.e., the (111), (100), (110), and (211) surfaces (Fig. 4*A*), using the TIP4P/2005 water model. This model can well reproduce the phase diagram of bulk ice polymorphs over a wide range of pressures and temperatures (46). Fig. 4*B* shows phase diagrams of the water layer on different fcc surfaces in the adsorption energy–lattice constant (E_{ads}–a) plane at T = 230 K.

The formation of bilayer ice is observed on the (111) surface when the value of E_{ads} is above a critical value E^c_{ads}, regardless of the lattice constant (Fig. 4*C*). As shown in Fig. 4*B*, E^c_{ads} tends to decrease first and then increase with increasing lattice constant a, yielding a minimum at a_{fcc} = 3.78 Å. It can be understood that the surface lattice constant (a_{surf}) of the (111) surface (the distance between 2 adjacent atoms at the surface) is 2.67 Å at

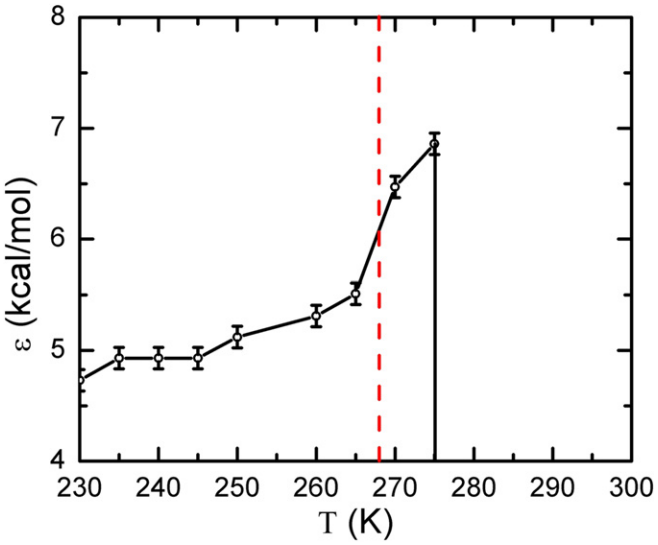

Fig. 3. A critical value of ε^c, namely, the value of ε at which the liquid–solid phase transition occurs, versus the system temperature. The red dashed line shows the melting temperature of the TIP4P/ice bulk ice (I_h).

a_{fcc} = 3.78 Å, which matches the length scale of the oxygen–oxygen distance in one layer of bilayer ice (2.73 Å in Fig. 2*D*). Formation of bilayer ice is also observed on the (100) surface (Fig. 4*D*) and on the (110) surface (Fig. 4*E*) when the value of E_{ads} is above a critical value E^c_{ads} with smaller lattice constants, i.e., $a_{fcc} < 4.43$ Å and $a_{fcc} < 4.30$ Å for the (100) surface and (110) surface (Fig. 4*B*), respectively. Interestingly, this critical adsorption energy of a single water molecule for the (110) surface is the largest among the (100), (110), and (111) surfaces, likely due to the relatively low symmetry of the (110) surface (Fig. 4*A*). In contrast to the other 3 surfaces, no bilayer ice is observed on the (211) surface for all a_{fcc} values (Fig. 4*B*). It can be understood that the outer layer of the (211) surface has atomic steps (Fig. 4*A*); thus, the water layer on the (211) surface exhibits pronounced buckling, which is energetically unfavorable for the formation of flat BHI. A similar buckled water layer can be observed on the (110) surface at large lattice constants (Fig. 4*B*). Although the outer layer of the (100) surface is atomically flat, no bilayer ice is observed on the surface at large lattice constants ($a_{fcc} > 4.30$ Å). Note that the (100) surface and BHI possess different surface symmetry (square versus hexagonal; Fig. 4*A* and Fig. 2*B*). Furthermore, the formation of BHI is inhibited for large lattice constants due to the lattice mismatch and different surface symmetry between the (100) surface and BHI.

On the (100) surface, in addition to BHI, flat monolayer square ice (fMSI) also forms when $E_{ads} > E^c_{ads}$ and when a_{fcc} is in the range from 3.78 to 4.17 Å (i.e., a_{surf} is in the range from 2.67 to 2.95 Å). Similar monolayer ice structures were observed in previous studies (7, 27, 47). A typical snapshot of fMSI is shown in Fig. 4*F* and *SI Appendix*, Fig. S18*A*. The computed oxygen–oxygen RDF $g_{OO}(r)$ illustrates the first sharp peak at ~2.82 Å (*SI Appendix*, Fig. S18*C*), corresponding to the measured lattice constant of monolayer square ice in graphene nanocapillaries (7). When the surface lattice constant of the (100) surface corresponds to the lattice constant of fMSI, strong interaction between the water molecules and the surface can promote the formation of fMSI since the surface can act as a template.

In contrast to those of the (100) and (111) surfaces, the outer layers of (211) and (110) surfaces exhibit atomic steps (Fig. 4*A*), which can strongly affect the formation of 2D ice. On the (110) surface at large lattice constants ($a_{fcc} > 3.91$ Å), the 2D ice exhibits pronounced buckling when $E_{ads} > E^c_{ads}$ (Fig. 4*B*). *SI Appendix*, Fig. S19*B* shows the TDP of oxygen atoms in the 2D ice with 2 peaks. A typical snapshot of the 2D ice is shown in Fig. 4*G* and *SI Appendix*, Fig. S19*A*. The green and blue oxygen atoms in Fig. 4*G* denote different locations along the *z* axis. The water molecules form square-like rings, indicating that the ice is puckered monolayer square-like ice (pMSI). A similar monolayer ice structure was observed in previous studies (27, 47). Two other pMSIs are observed on the (211) surface, while no bilayer ice can form on the surface (Fig. 4*B*). For a_{fcc} values ranging from 3.78 to 3.91 Å, a new monolayer ice is formed on the (211) surface when $E_{ads} > E^c_{ads}$. As shown in Fig. 4*H*, the water molecules in the 2D ice exhibit square rings. We named the 2D ice pMSI-II. In a unit cell of pMSI-II (yellow rectangle in Fig. 4*H*), there is one quadrilateral parallel to the *xy* panel and 4 quadrilaterals nonparallel to the *xy* panel. The TDP of oxygen atoms in pMSI-II appears to have 3 peaks (*SI Appendix*, Fig. S20*B*) because the right-column oxygen atoms in the bottom layer (right blue balls in Fig. 4*H*) are slightly higher than the left ones in the bottom layer (left blue balls in Fig. 4*H*) by ~0.4 Å.

For a_{fcc} values ranging from 3.91 to 4.43 Å, another pMSI (named pMSI-III here) forms spontaneously on the surface, as shown in Fig. 4*I*, when $E_{ads} > E^c_{ads}$. The TDP of oxygen atoms in pMSI-III is shown in *SI Appendix*, Fig. S21*B*, where 3 peaks appear. In the unit cell of pMSI-III, all 3 quadrilaterals are not parallel to the *xy* panel (rectangle in Fig. 4*I*). The $g_{OO}(r)$ functions of the 3 pMSI structures are shown in *SI Appendix*, Figs. S19*C*, S20*C*, and S21*C*, respectively. It appears that all 3 pMSIs exhibit a sharp peak at ~2.79 Å, very close to the measured value of fMSI (7). The high number of pMSIs observed on surfaces is mainly due to the weak hydrogen-bonding interaction.

Discussions and Conclusion

The formation of BHI on surfaces previously achieved in the laboratory mostly involved surfaces having weak interactions with water (32, 34, 35). Here, our study focuses on the formation of BHI on surfaces having stronger interaction (than previously considered) with water. More specifically, the growth of bilayer ice has been widely observed experimentally on graphene (32), Pt(111) surface (35), Ru(0001) substrate (35), and Au (111) surface (34) without confinement. Note that the nearest atom–atom distances for the graphene, Pt(111) surface, Ru(0001) substrate, and Au(111) surface are 1.42, 2.78, 2.72, and 2.88 Å, respectively, indicating that the structure of the substrate is not the most important factor. Note also that most experiments were done at low temperature. For graphene, thin films of water were deposited on the substrate at temperatures ranging from 20 to 152 K. The BHI was only observed for $T < 135$ K, while cubic ice Ic was observed at higher temperature. For comparison, the BHI can be observed on the Pt(111) surface and Ru(0001) substrate (35), even for $T > 135$ K. It is known that Pt [E_{ads} = 7.0 kcal/mol (44)] and Ru [E_{ads} = 9.4 kcal/mol (44)] are much more hydrophilic than graphene [E_{ads} = 0.9 kcal/mol (48)]. Hence, these experimental results are already consistent with our predictions.

Scanning tunneling microscopy was used to investigate water deposition on Ru(0001), Pt(111), and Au(111) substrates, and the measurements were all done at low temperature [for Ru and Pt, $T < 150$ K (35); and for Au, $T < 120$ K (34)]. In addition to BHI, MD simulations (49) and density functional theory study (50) show that fMSI can form on the Pt(100) surface [a_{fcc} = 3.92 Å, E_{ads} = 9.9 kcal/mol (51)] and on the ceria(100) surface [the neighboring surface oxygen ions are 2.74 Å, E_{ads} = 21.7 kcal/mol (50)], which are all consistent with our predictions. Atomic force microscopy (AFM) was also used to study the growth and morphology of ice films on the cleavage surface of mica (52). Between −20 and −10 °C and at a relative humidity of ~83%, the film, consisting of a solid ice layer ~7 Å thick, covered by a liquid-like layer 50 ± 5 Å thick, was observed. The solid-ice layer was suggested as a bilayer of ice I_h since the height of the solid-ice layer corresponds to that of the bilayers of ice I_h. However, bilayers of ice I_h typically have numerous dangling H and are likely not very stable. Interestingly, the height of the BHI is also ~7 Å (Fig. 2*C*), but without any dangling H. Hence, we speculate that the solid-ice layer observed in the AFM experiment could be

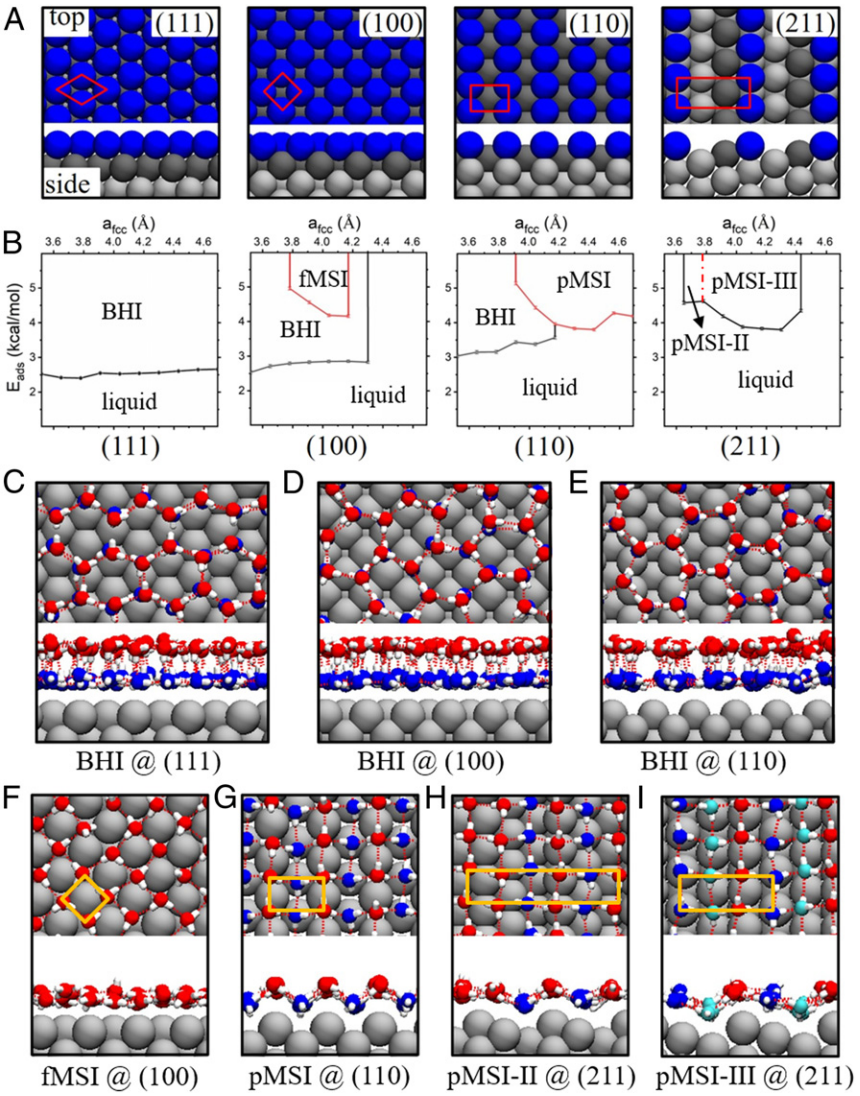

Fig. 4. (*A*) Top and side views of the 4 fcc surfaces considered. Atoms are colored according to their *z* coordinate. Red boxes highlight the symmetry of the surface unit cells. (*B*) Sketch of the phase diagrams of 2D ice on the 4 different fcc surfaces considered in the plane of adsorption energy E_{ads} versus the lattice parameter a_{fcc}. (*C*–*E*) Top and side views of BHI formed on the (111), (100), and (110) surfaces, respectively. (*F*) Top and side views of fMSI formed on the (100) surface. (*G*) Top and side views of pMSI formed on the (110) surface. (*H*) Top and side views of pMSI-II formed on the (211) surface. (*I*) Top and side views of pMSI-III formed on the (211) surface. Yellow boxes in *F*–*I* highlight the unit cells of the 2D ice formed on the surface.

the BHI, especially considering the hydrophilic nature of the mica surface. If the observed solid-ice layer is indeed the BHI, a relative humidity of 83% applied indicates again that the pressure would have little influence on the formation of BHI.

In conclusion, we have investigated the effect of the interplay between surface morphology and hydrophobicity on the formation of 2D ices on either a smooth surface or fcc crystalline surfaces with a wide range of water adsorption energies and lattice parameters. We find that BHI can form directly from liquid water on the surfaces near room temperature without nanoscale confinement. The wettability of the surfaces plays a key role in the liquid-to-bilayer ice transition. For the water–surface interaction parameter ε, there is a critical value above which the liquid-to-bilayer ice transition on the surface can be observed. Indeed, bilayer ice whose melting temperature is above that of bulk ice (I_h) can even form on a superhydrophilic surface. The formation of bilayer ice on surfaces is attributed to the satisfaction of the Bernal–Fowler ice rules and the strong interaction between water and the surface, which can compensate for the entropy loss due to the freezing transition. Above 280 K, the bilayer ice can no longer form on the surface. The generic formation of 2D ices without confinement revealed in this work will hopefully motivate future experimental studies of 2D ice formation on a variety of realistic surfaces.

Methods

We considered a water slab that includes 213 water molecules and is in contact with a surface. Here, our focus was not placed on specific metallic surfaces, but rather on generic insight into 2D ice formation on model surfaces. To this end, we considered a smooth surface, as well as 4 different crystallographic planes of a fcc crystal, namely, the (111), (100), (110), and (211) surfaces, each with unique atomic roughness and symmetry of the exposed crystalline layer. The TIP4P/ice potential was used to describe the water–water interaction (53). This model has been validated by many researchers in their studies of the structure, thermodynamic properties, and crystallization of water (53–58). In particular, the melting point of the TIP4P/ice model hexagonal ice is $T_m = 268 \pm 2$ K (53), very close to that of the bulk ice I_h. The water–smooth-surface interaction was modeled by a 9-3 Lennard–Jones potential function, $U(r) = \varepsilon\left(\left(\frac{\sigma}{r}\right)^9 - \left(\frac{\sigma}{r}\right)^3\right)$, where the parameter $\sigma = 2.263$ Å, while for the 4 different crystallographic planes of an fcc crystal, the water–atom interaction was modeled by a 12-6 Lennard–Jones potential function, $U(r) = 4\varepsilon\left(\left(\frac{\sigma}{r}\right)^{12} - \left(\frac{\sigma}{r}\right)^6\right)$, where the parameter $\sigma = 3.2$ Å. The parameter ε was adjusted to describe the different degrees of surface hydrophobicity. Long-range electrostatic interactions were treated by using the particle–particle particle–mesh method with a real-space cutoff distance of 10 Å. The 10-Å cutoff distance was also applied to the van der Waals interactions (59). A slab-like simulation box, relatively thin in the *x* direction ($l_x = 30$ Å) and relatively long in the *y* ($l_y = 100$ Å) and *z* directions ($l_z = 100$ Å), was adopted. Periodic boundary conditions were imposed in both the *x* and *y* directions, such that the water slab was infinite in the *x* direction. The MD simulations

were performed by using the GROMACS package (Version 4.6.5) (60) in the constant-volume and temperature (*NVT*) ensemble with a time step of 1.5 fs. The temperature T was controlled within a range from 230 K to 300 K. For a given T and ε, the simulation time was 30 ns. Three other water models, i.e., TIP4P/2005 (39), monatomic water model mW (40), and HBP polarizable water model (41), were also considered to ensure no model dependence in key physical phenomena. Overall, a total of ~2,000 MD simulations were performed.

ACKNOWLEDGMENTS. X.C.Z. and J.S.F. are supported by National Science Foundation Grant CHE-1665324. X.C.Z. is also supported by the Nebraska Center for Energy Sciences Research at University of Nebraska–Lincoln. J.W. is supported by 973 Program Grant 2013CB933000; National Natural Science Foundation of China Grants 51436004 and 21421061; and Strategic Priority Research Program of the Chinese Academy of Sciences Grant XDA09020000. The computational work was performed at the University of Nebraska Holland Computing Center.

1. J. Carrasco, A. Hodgson, A. Michaelides, A molecular perspective of water at metal interfaces. *Nat. Mater.* **11**, 667–674 (2012).
2. C. Tanford, The hydrophobic effect and the organization of living matter. *Science* **200**, 1012–1018 (1978).
3. D. Chandler, Interfaces and the driving force of hydrophobic assembly. *Nature* **437**, 640–647 (2005).
4. C. Zhu, H. Li, Y. Huang, X. C. Zeng, S. Meng, Microscopic insight into surface wetting: Relations between interfacial water structure and the underlying lattice constant. *Phys. Rev. Lett.* **110**, 126101 (2013).
5. J. Rafiee *et al.*, Wetting transparency of graphene. *Nat. Mater.* **11**, 217–222 (2012).
6. S. P. Koenig, N. G. Boddeti, M. L. Dunn, J. S. Bunch, Ultrastrong adhesion of graphene membranes. *Nat. Nanotechnol.* **6**, 543–546 (2011).
7. G. Algara-Siller *et al.*, Square ice in graphene nanocapillaries. *Nature* **519**, 443–445 (2015).
8. A. Michaelides, K. Morgenstern, Ice nanoclusters at hydrophobic metal surfaces. *Nat. Mater.* **6**, 597–601 (2007).
9. A. Hodgson, S. Haq, Water adsorption and the wetting of metal surfaces. *Surf. Sci. Rep.* **64**, 381–451 (2009).
10. H. Ogasawara *et al.*, Structure and bonding of water on Pt(111). *Phys. Rev. Lett.* **89**, 276102 (2002).
11. C. Zhu *et al.*, Characterizing hydrophobicity of amino acid side chains in a protein environment via measuring contact angle of a water nanodroplet on planar peptide network. *Proc. Natl. Acad. Sci. U.S.A.* **113**, 12946–12951 (2016).
12. S. Meng, Z. Zhang, E. Kaxiras, Tuning solid surfaces from hydrophobic to superhydrophilic by submonolayer surface modification. *Phys. Rev. Lett.* **97**, 036107 (2006).
13. C. Wang *et al.*, Stable liquid water droplet on a water monolayer formed at room temperature on ionic model substrates. *Phys. Rev. Lett.* **103**, 137801 (2009).
14. J. Liu *et al.*, Distinct ice patterns on solid surfaces with various wettabilities. *Proc. Natl. Acad. Sci. U.S.A.* **114**, 11285–11290 (2017).
15. J. Chen, G. Schusteritsch, C. J. Pickard, C. G. Salzmann, A. Michaelides, Two dimensional ice from first principles: Structures and phase transitions. *Phys. Rev. Lett.* **116**, 025501 (2016).
16. K. Koga, X. C. Zeng, H. Tanaka, Freezing of confined water: A bilayer ice phase in hydrophobic nanopores. *Phys. Rev. Lett.* **79**, 5262–5265 (1997).
17. J. Slovak, H. Tanaka, K. Koga, X. C. Zeng, Computer simulation of bilayer ice: Structures and thermodynamics. *Physica A* **319**, 163–174 (2003).
18. R. Zangi, A. E. Mark, Bilayer ice and alternate liquid phases of confined water. *J. Chem. Phys.* **119**, 1694–1700 (2003).
19. S. H. Han, M. Y. Choi, P. Kumar, H. E. Stanley, Phase transitions in confined water nanofilms. *Nat. Phys.* **6**, 685–689 (2010).
20. N. Kastelowitz, J. C. Johnston, V. Molinero, The anomalously high melting temperature of bilayer ice. *J. Chem. Phys.* **132**, 124511 (2010).
21. J. Bai, X. C. Zeng, Polymorphism and polyamorphism in bilayer water confined to slit nanopore under high pressure. *Proc. Natl. Acad. Sci. U.S.A.* **109**, 21240–21245 (2012).
22. W. Zhu *et al.*, Two-dimensional interlocked pentagonal bilayer ice: How do water molecules form a hydrogen bonding network? *Phys. Chem. Chem. Phys.* **18**, 14216–14221 (2016).
23. R. Zangi, A. E. Mark, Monolayer ice. *Phys. Rev. Lett.* **91**, 025502 (2003).
24. W. H. Zhao, J. Bai, L. F. Yuan, J. L. Yang, X. C. Zeng, Ferroelectric hexagonal and rhombic monolayer ice phases. *Chem. Sci.* **5**, 1757–1764 (2014).
25. M. Jia, W. H. Zhao, L. F. Yuan, New hexagonal-rhombic trilayer ice structure confined between hydrophobic plates. *Chin. J. Chem. Phys.* **27**, 15–19 (2014).
26. N. Giovambattista, P. J. Rossky, P. G. Debenedetti, Phase transitions induced by nanoconfinement in liquid water. *Phys. Rev. Lett.* **102**, 050603 (2009).
27. W. H. Zhao *et al.*, Highly confined water: Two-dimensional ice, amorphous ice, and clathrate hydrates. *Acc. Chem. Res.* **47**, 2505–2513 (2014).
28. J. Hu, X. D. Xiao, D. F. Ogletree, M. Salmeron, Imaging the condensation and evaporation of molecularly thin films of water with nanometer resolution. *Science* **268**, 267–269 (1995).
29. M. Odelius, M. Bernasconi, M. Parrinello, Two dimensional ice adsorbed on mica surface. *Phys. Rev. Lett.* **78**, 2855–2858 (1997).
30. H. Li, X. C. Zeng, Two dimensional epitaxial water adlayer on mica with graphene coating: An ab initio molecular dynamics study. *J. Chem. Theory Comput.* **8**, 3034–3043 (2012).
31. P. B. Miranda, L. Xu, Y. R. Shen, M. Salmeron, Icelike water monolayer adsorbed on mica at room temperature. *Phys. Rev. Lett.* **81**, 5876–5879 (1998).
32. G. A. Kimmel *et al.*, No confinement needed: Observation of a metastable hydrophobic wetting two-layer ice on graphene. *J. Am. Chem. Soc.* **131**, 12838–12844 (2009).
33. K. Koga, H. Tanaka, X. C. Zeng, First-order transition in confined water between high-density liquid and low-density amorphous phases. *Nature* **408**, 564–567 (2000).
34. D. Stacchiola *et al.*, Water nucleation on gold: Existence of a unique double bilayer. *J. Phys. Chem. C* **113**, 15102–15105 (2009).
35. S. Maier, B. A. J. Lechner, G. A. Somorjai, M. Salmeron, Growth and structure of the first layers of ice on Ru(0001) and Pt(111). *J. Am. Chem. Soc.* **138**, 3145–3151 (2016).
36. W. Xiong, J. Z. Liu, Z. L. Zhang, Q. S. Zheng, Control of surface wettability via strain engineering. *Acta Mech. Sin.* **29**, 543–549 (2013).
37. I. Brovchenko, A. Geiger, A. Oleinikova, D. Paschek, Phase coexistence and dynamic properties of water in nanopores. *Eur. Phys. J E Soft Matter* **12**, 69–76 (2003).
38. M. Watkins, J. VandeVondele, B. Slater, Point defects at the ice (0001) surface. *Proc. Natl. Acad. Sci. U.S.A.* **107**, 12429–12434 (2010).
39. J. L. F. Abascal, C. Vega, A general purpose model for the condensed phases of water: TIP4P/2005. *J. Chem. Phys.* **123**, 234505 (2005).
40. V. Molinero, E. B. Moore, Water modeled as an intermediate element between carbon and silicon. *J. Phys. Chem. B* **113**, 4008–4016 (2009).
41. H. Jiang, O. A. Moultos, I. G. Economou, A. Z. Panagiotopoulos, Hydrogen-bonding polarizable intermolecular potential model for water. *J. Phys. Chem. B* **120**, 12358–12370 (2016).
42. I. Brovchenko, A. Geiger, A. Oleinikova, Water in nanopores. I. Coexistence curves from Gibbs ensemble Monte Carlo simulations. *J. Chem. Phys.* **120**, 1958–1972 (2004).
43. I. Brovchenko, A. Oleinikova, Water in nanopores: III. Surface phase transitions of water on hydrophilic surfaces. *J. Phys. Chem. C* **111**, 15716–15725 (2007).
44. S. Meng, E. G. Wang, S. W. Gao, Water adsorption on metal surfaces: A general picture from density functional theory studies. *Phys. Rev. B Condens. Matter Mater. Phys.* **69**, 195404 (2004).
45. C. Vega, J. L. F. Abascal, I. Nezbeda, Vapor-liquid equilibria from the triple point up to the critical point for the new generation of TIP4P-like models: TIP4P/Ew, TIP4P/2005, and TIP4P/ice. *J. Chem. Phys.* **125**, 34503 (2006).
46. Y. Huang *et al.*, A new phase diagram of water under negative pressure: The rise of the lowest-density clathrate s-III. *Sci. Adv.* **2**, e1501010 (2016).
47. Y. Zhu, F. Wang, J. Bai, X. C. Zeng, H. Wu, Compression limit of two-dimensional water constrained in graphene nanocapillaries. *ACS Nano* **9**, 12197–12204 (2015).
48. R. R. Q. Freitas, R. Rivelino, F. de Brito Mota, C. M. C. de Castilho, DFT studies of the interactions of a graphene layer with small water aggregates. *J. Phys. Chem. A* **115**, 12348–12356 (2011).
49. D. T. Limmer, A. P. Willard, P. Madden, D. Chandler, Hydration of metal surfaces can be dynamically heterogeneous and hydrophobic. *Proc. Natl. Acad. Sci. U.S.A.* **110**, 4200–4205 (2013).
50. T. Kropp, J. Paier, J. Sauer, Interactions of water with the (111) and (100) surfaces of ceria. *J. Phys. Chem. C* **121**, 21571–21578 (2017).
51. J. L. C. Fajín, M. N. D S Cordeiro, J. R. B. Gomes, Density functional theory study of the water dissociation on platinum surfaces: General trends. *J. Phys. Chem. A* **118**, 5832–5840 (2014).
52. H. Bluhm, M. Salmeron, Growth of nanometer thin ice films from water vapor studied using scanning polarization force microscopy. *J. Chem. Phys.* **111**, 6947–6954 (1999).
53. J. L. F. Abascal, E. Sanz, R. García Fernández, C. Vega, A potential model for the study of ices and amorphous water: TIP4P/Ice. *J. Chem. Phys.* **122**, 234511 (2005).
54. E. B. Moore, E. de la Llave, K. Welke, D. A. Scherlis, V. Molinero, Freezing, melting and structure of ice in a hydrophilic nanopore. *Phys. Chem. Chem. Phys.* **12**, 4124–4134 (2010).
55. J. C. Johnston, N. Kastelowitz, V. Molinero, Liquid to quasicrystal transition in bilayer water. *J. Chem. Phys.* **133**, 154516 (2010).
56. L. Jensen *et al.*, Calculation of liquid water-hydrate-methane vapor phase equilibria from molecular simulations. *J. Phys. Chem. B* **114**, 5775–5782 (2010).
57. V. Buch, H. Groenzin, I. Li, M. J. Shultz, E. Tosatti, Proton order in the ice crystal surface. *Proc. Natl. Acad. Sci. U.S.A.* **105**, 5969–5974 (2008).
58. E. G. Noya, C. Menduina, J. L. Aragones, C. Vega, Equation of state, thermal expansion coefficient, and isothermal compressibility for ices Ih, II, III, V, and VI, as obtained from computer simulation. *J. Phys. Chem. C* **111**, 15877–15888 (2007).
59. M. Deserno, C. Holm, How to mesh up Ewald sums. I. A theoretical and numerical comparison of various particle mesh routines. *J. Chem. Phys.* **109**, 7678–7693 (1998).
60. B. Hess, C. Kutzner, D. van der Spoel, E. Lindahl, GROMACS 4: Algorithms for highly efficient, load-balanced, and scalable molecular simulation. *J. Chem. Theory Comput.* **4**, 435–447 (2008).